



Cite this: *Phys. Chem. Chem. Phys.*,
2024, 26, 1385

Breaking the size constraint for nano cages using annular patchy particles†

Vikki Anand Varma,  Simmie Jaglan, Mohd Yasir Khan  and Sujin B. Babu  *

Engineering structures like nanocages, shells, and containers, by self-assembly of colloids is a challenging problem. One of the main challenges is to define the shape of the individual subunits to control the radius of the closed shell structures. In this work, we have proposed a simple model for the subunit, which comprises a spheroidal or spherical hardcore decorated with an annular patch. The self-assembly of these building blocks leads to the formation of monodispersed spherical cages (close shells) or containers (curved clusters). For a spheroid with a given bonding range, the curvature of the shell is analytically related to only the patch angle of the building blocks and independent of the shape of the subunits. This model with only one control parameter can be used to engineer cages with the desired radius, which also have been verified using thermodynamic calculations. In the phase diagram of the system, 4 phases are identified which includes gas, closed shell, partially closed (containers) shell and percolated structures. When the diameters of the spherical cages formed are small, we observe an icosahedral symmetry similar to virus capsids. We also observed that the kinetics of the cage formation is very similar to the nucleation and growth kinetics of viruses and is the key factor in determining the yield of closed shells.

Received 1st August 2023,
Accepted 6th December 2023

DOI: 10.1039/d3cp03681b

rsc.li/pccp

1 Introduction

With the advancement in our understanding of nanoscale phenomena, researchers have found ways to synthesize different types of nanocages. The possible uses of these cages are in targeted drug delivery,^{1,2} nanoreactors,³ nanocontainers⁴ etc. Recently it was shown that using nanocages it is possible to trap viruses, thus giving us a new method of treatment for viral infections.⁵ The close nanocluster has been studied experimentally^{6–8} as well as by simulation.^{9–12} Experimentally, nanocages are formed either by biological molecules^{13,14} or through a chemical route.^{15–17} Patchy colloidal particles with directional interaction have been used as a model for the aggregation of supramolecular structures,^{18,19} water molecules,²⁰ virus capsids,¹⁰ engineering superlattices,^{21,22} etc. Few studies have focused on patchy particles to mimic the cage formation in the nanoscale,^{23–28} which leads to highly mono-dispersed structures for a very specific type of anisotropic particle.²⁸ It is challenging to use different shapes of patchy particles and to control the size of the shell-like structures^{29,30} simultaneously. These models have been proposed with subunits having particular complex shape and size properties, which leads to highly

specific structures. Many parameters are required to control the properties of the proposed structures. In the present work, we have proposed a simple annular patchy potential leading to the formation of monodisperse spherical shells by tuning only the patch angle, irrespective of the shape of the anisotropic spheroids. The present model of annular patches thus addresses the size constraint challenges of the closed shell irrespective of the shape of the patchy particles. This model gives flexibility for the rearrangement, which leads to a liquid-like structure over the surface of the closed shells. This may be the reason behind the high stability of the shells. These structures will find applications in vaccine production, acting as nanoreactors,³ drug delivery systems, etc.^{1,2}

In the biological world we know that the subunits of certain kinds of viruses aggregate together to form spherical closed structures with icosahedral symmetry. At very low temperature, the nucleation rates of these subunits are very high and the yield of the closed shells falls leading to partially open shells, as reported in the kinetic study of the shell growth of viral capsids³¹ in solution. It was also shown that when the number of subunits being part of the closed structure increases, the size of the shell increases. It was also observed that a subunit having six near neighbors increases dramatically in comparison to the subunits having five near neighbors.³² Mosayeb *et al.*⁹ studied the similar structures, by letting the subunits move on the surface of a sphere whose radius was fixed. They showed that for small sphere radius the subunit was distributed on the

Out of Equilibrium Group, Department of Physics, Indian Institute of Technology Delhi, New Delhi 110016, India. E-mail: sujin@physics.iitd.ac.in

† Electronic supplementary information (ESI) available. See DOI: <https://doi.org/10.1039/d3cp03681b>

surface of the sphere with icosahedral symmetry similar to virus capsids, and as the diameter increased the symmetry vanished. In our present model, through self assembly we were able to observe that annular patchy particles formed closed structures through self assembly similar to spherical viruses. The closed structure formed in the present model shows icosahedral symmetry if the diameter is comparable to the size of the subunit and as the diameter increases the symmetry breaks down.

To study the kinetics and structure of the system we have used the Brownian cluster dynamics (BCD)³³ method, which is a well-known kinetic Monte-Carlo method. Using Brownian cluster dynamics, a variety of colloidal systems have been modeled with discontinuous potential^{33–35} for studying both irreversible^{36–40} and reversible^{41–44} systems. It was shown that the structure, kinetics and dynamics of BCD and event driven molecular dynamics simulation are the same.⁴²

In the simulation section, we discuss in detail the proposed annular potential, along with the cluster formation and dynamics undertaken by the subunits in the kinetic Monte Carlo technique (BCD). In the Results section, the formation of cages, and its dependence on the volume fraction temperature and various other parameters are explored in detail. The radius of the cages formed in the *NVT* ensemble is calculated analytically as well as compared with the modified Gibbs ensemble Monte Carlo method. The kinetics of the cage formation along with the local order of the cages are studied followed by conclusion in the last section.

2 Model and simulation method

In the present work, the subunits considered are spheroids (oblate, prolate) and spheres with an aspect ratio $p = a/b$, where a and b are the semi-major and semi-minor axes. All the subunits have the same volume $\pi d^3/6$, where d is the diameter of the sphere, which is kept as unity in the present work.

The subunits interact with each other through a hard-core potential and an annular patch, where patch orientation \hat{n} , is considered along the direction of the symmetry axis of the spheroids. We define the annular patch by a modified Kern-Frenkel potential, given as,

$$U_{i,j} = \begin{cases} -u \cdot \sigma_{ij}(\mathbf{r}_{ij}; \hat{\mathbf{n}}_i; \hat{\mathbf{n}}_j) \cdot \chi_{ij}(\mathbf{r}_{ij}; \hat{\mathbf{n}}_i; \hat{\mathbf{n}}_j) & \text{Hardcore} \\ \infty & \text{overlap} \end{cases} \quad (1)$$

where $\hat{\mathbf{n}}_i, \hat{\mathbf{n}}_j$ is the patch vector and \mathbf{r}_{ij} is the distance between the center of mass of subunits i and j , respectively. u is the depth of the square well potential with the interaction range ε , where we have the energy scaled in terms of $u/k_B T$. We define $h_{ij}(\mathbf{r}_{ij}; \hat{\mathbf{n}}_i; \hat{\mathbf{n}}_j)$ as the distance from the surface of the spheroid where the patches are attached, which is calculated by using the ellipsoids contact function (ECF).³⁵ σ_{ij} and χ_{ij} are defined as,

$$\sigma_{ij} = \begin{cases} 1 & h_{i,j} < \varepsilon \\ 0 & \text{Otherwise} \end{cases} \quad (2)$$

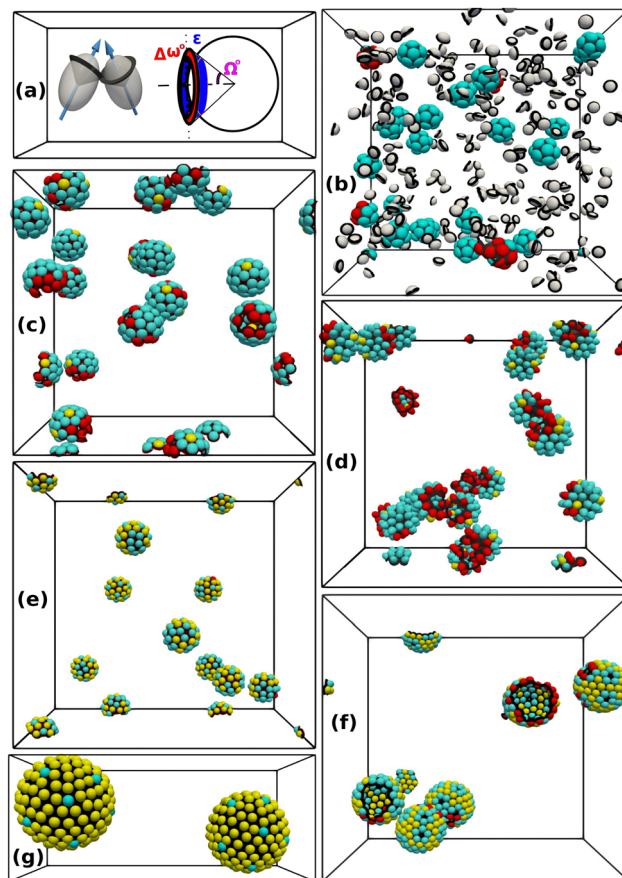


Fig. 1 (a) Subunits with oblate hardcore (gray color), along with annular patches shown as (black) ring-like structures and the arrows passing through the symmetry axis of the subunits represent the patch vector. To the right a spherical subunit is shown where Ω° is the patch angle, $\Delta\omega^\circ$ is the annular width and ε is the interaction range. All the subunits represented in grey color have less than 4 bonded neighbors. While red subunits have bonded neighbors < 5 . Cyan and yellow subunits have 5 and 6 bonded neighbors, respectively. (b) Oblate hardcore with annular patches forming mono-dispersed structures with icosahedral symmetry, shown at $k_B T/u = 0.115$ $\Omega^\circ = 60^\circ$, $\varepsilon = 0.25$ and $\Delta\omega^\circ = 3^\circ$. Fully evolved closed shell is shown at $k_B T/u = 0.115$ $\Omega^\circ = 74^\circ$, $\varepsilon = 0.25$ and $\Delta\omega^\circ = 3^\circ$, with (c) oblate ellipsoid, (d) prolate ellipsoid and (e) spherical subunits. In these systems, the small disordered clusters (monomers, dimers, trimers) are removed for better visualization. (f) Clusters formed for spherical subunits at $k_B T/u = 0.137$ for $\Omega^\circ = 79.6^\circ$, $\varepsilon = 0.1$ and $\Delta\omega^\circ = 4.5^\circ$, where we can also observe voids at the center of the pentagonally arranged spherical subunits. (g) Very large shells of spherical subunits formed at $k_B T/u = 0.142$ for $\Omega^\circ = 82^\circ$, $\varepsilon = 0.4$ and $\Delta\omega^\circ = 3^\circ$.

$$\chi_{ij} = \begin{cases} 1 & \cos(\Omega^\circ + \Delta\omega^\circ) \geq \hat{\mathbf{r}}_{ij} \cdot \hat{\mathbf{n}}_i \geq \cos(\Omega^\circ - \Delta\omega^\circ), \\ & \cos(\Omega^\circ + \Delta\omega^\circ) \geq \hat{\mathbf{r}}_{ij} \cdot \hat{\mathbf{n}}_j \geq \cos(\Omega^\circ - \Delta\omega^\circ) \\ 0 & \text{Otherwise} \end{cases} \quad (3)$$

where $\Delta\omega^\circ$ is the angular width of the patch located at a semi-conic angle Ω° , along the patch vector of the subunit, as shown in Fig. 1(a). When $\sigma_{ij} = 1$, it means that the two ellipsoids are within a square well potential with range ε , and $\chi_{ij} = 1$, when only the annular region overlaps.

To study the structure and kinetics of the self-assembly, we have used the Brownian cluster dynamics (BCD)³³ simulation technique, a kinetic *NVT* Monte-Carlo (MC) scheme. The simulation starts with N number of particles (subunits), randomly scattered in a cubical box of length L . The volume fraction of the system is defined as, $\phi = \frac{\pi d^3 N}{6L^3}$. A simulation step consists of two parts of a movement step followed by a cluster construction step. For the movement step, we select subunits randomly $2N$ times and then either rotate the subunit with respect to the director or translate the center of mass of the subunit, with equal probability. In this way, on average every particle has performed one rotational and one translational movement step. For the translational movement, a center of mass of the subunit is displaced through a constant step length S_T , along a random direction. Similarly, for the rotational step, the unit vector \hat{n} is rotated with a fixed step length $S_R = |\hat{n} - \hat{n}'|$, where \hat{n} and \hat{n}' are the orientation of the director of the subunit before and after the rotation step. Prabhu *et al.*³⁴ have shown that S_R and S_T follow the relation $S_R^2 = 2S_T^2$. For the spheroidal particle, the translational and rotational step size are scaled with respect to the Perrins factor, which has been shown to mimic the single particle diffusion accurately.³⁵ If the movement of the subunit leads to the overlap of the hardcore particle or breakage of a bond, that movement step is rejected. After the movement step, we perform a cluster construction step. When the annular patches of the subunit are within each others range a bond is formed with a probability α .¹⁸ If the bond already exists, it is broken with a probability β_b , such that the probability for a bond to exist is given by $P = \alpha/(\alpha + \beta_b)$ such that $P = 1 - e^{-u/k_B T}$,³³ where $u/k_B T$ is a positive number. All the subunits connected through the bonds are defined as a cluster such that a monomer is a cluster of size 1. The movement step followed by a cluster construction step is considered as a simulation step. The relation between simulation step t_{sim} and physical time t_{phy} , is given as $t_{phy}/t_0 = S_T^2 \cdot t_{sim}$.³³ Such that t_0 is the time taken for a single sphere to diffuse through its own diameter. By using bigger S_T , we can achieve larger t_{phy} for the same number of simulation steps. But bigger S_T can also lead to more rejection, leading to nonphysical diffusivity and kinetics of the system. In the present work S_T is set at $0.01d$,³⁵ which keeps the dynamics accurate without compromising the computational efficiency. The kinetics is explored to the order of 10^4 physical time, with the number of subunits ranging between $N = 1000$ – 4000 .

3 Results

3.1 Structural properties

Fig. 1 shows the typical structures formed for different parameter ranges, along with different kinds of subunit as given in the caption. Red color is used to indicate subunits having less than 5 bonded neighbors. The cyan and yellow-colored subunits have 5 and 6 bonded neighbors, respectively. In Fig. 1 the grey subunits correspond to small size clusters (monomers,

dimers, trimers). These small clusters have been removed in the following images for better visualisation. In Fig. 1(b) we observe highly monodispersed clusters having icosahedral symmetry, formed at $\Omega = 60^\circ$. The clusters consist of 12 subunits ($c_s = 12$), where each subunit has five bonded neighbours. As we increase Ω , the cluster size increases and the shells formed have subunits with six bonded neighbors (Fig. 1(c)–(g)), alongside five bonded neighbors. This is expected, as for the formation of spherical closed structures, a combination of pentagons (5 bonded subunits) and hexagons (6 bonded subunits) is needed, an example being a virus capsid.⁹ For $\Omega = 74$, the formation of mono-dispersed closed shells can be observed, which is shown for the systems having Fig. 1(c) oblate, (d) prolate, and (e) spherical-shaped subunits. The shells are closed irrespective of the shape of the hardcore, with the average number of subunits per shell $\bar{c}_s = 42$. In Fig. 1(f) and (g), the snapshots show larger closed structures with the number of subunits $c_s = 96$ and $c_s = 165$, formed at $\Omega^\circ = 79.6^\circ$ and 82° , respectively. In all the snapshots, it is observed that the closed structures formed are monodisperse in nature with respect to the radius of the closed shell structures.

In the present study we observe four different types of clusters in the system. The clusters having subunits with random orientation of the patch vector are designated as disordered or gas clusters (G), closed shell structures (C), partially closed shells (COD) and percolated clusters (P). The appearance of these structures at different temperatures and volume fractions ϕ ,⁴⁵ obtained from the simulations, is shown in Fig. 2(a). A typical system with a particular annular patch having $\Omega^\circ = 74$, $\Delta\omega = 4.5^\circ$, and $\varepsilon = 0.25$ is chosen in Fig. 2. The specific parameters were selected such that the shells formed were neither too large, which would lead to a longer convergence time of the system to the final equilibrium, nor too small (Fig. 1(b)) such that the diameter of the shell is comparable or bigger than the size of the constituent subunits. The self assembled closed shell was identified by calculating the distance to the subunit from the center of mass r_{cm} (radius of the closed shell) and the center of curvature of the curved cluster r_{cc} defined as the point for where all the subunits are equidistant and the distance will be equal to the radius of curvature of the closed shell. If the difference between $|r_{cm} - r_{cc}|/d$ reaches a steady state, we identify the cluster as a closed shell.

In Fig. 2(a) for high temperature $k_B T/u \geq 0.2$ and low concentration regime $\phi \leq 0.3$, the system is dominantly occupied by the monomers and the small size disordered clusters mostly consist of dimers and trimers represented by G in Fig. 2(a). For $\phi \leq 0.08$ when the temperature is 0.16, along with disordered clusters we observe the formation of one or two closed structures, which is identified as the C region in Fig. 2(a). When we further reduce the temperature to 0.14, the life time of the bond increases, and the system tries to form multiple closed structures leading to partially closed structures along with disordered clusters shown as the region COD. When the difference between the center of mass and the center of curvature of the cluster is < 0.1 we identify it in the C region, otherwise it will be in the COD region. For $\phi > 0.3$ we have not observed the C region. At a low temperature < 0.2 and $\phi \sim 0.4$

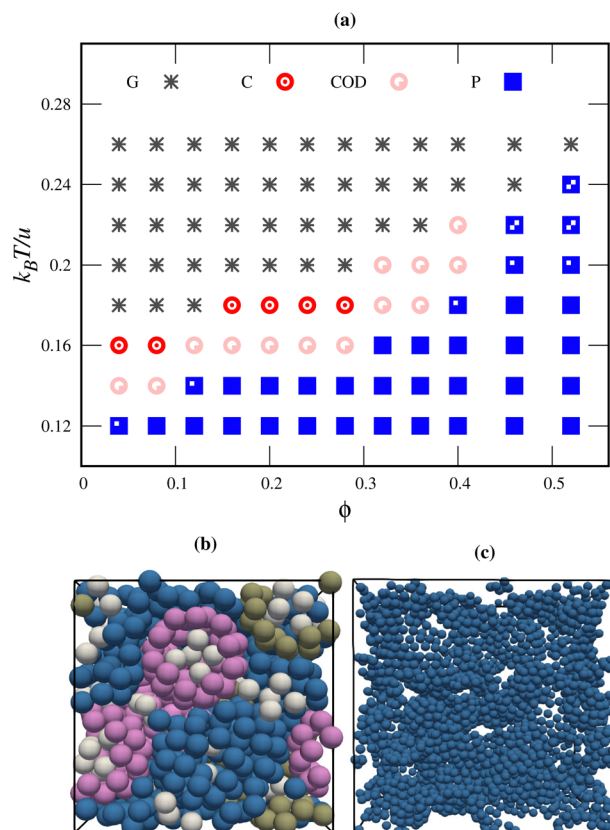


Fig. 2 (a) Different region identified in the $k_B T/u$ – ϕ plane, obtained in the NVT ensemble for spherical ($p = 1$) shaped subunits with patch angle $\Omega^\circ = 74$, width $\Delta\omega^\circ = 4.5$ and range $\varepsilon = 0.25$. Here, G (grey stars) represents the region having disordered clusters ranging from small (monomers, dimers, etc) to large size clusters. C (red circles) represents the region having closed shells, coexisting with the small-size clusters (monomers, dimers, trimers). The COD (pink circles) region is dominated by the presence of open shells along with closed shells and disordered clusters. The P (blue square) region represents percolated clusters. (b) Snapshot for the system at $\phi = 0.4$ and $k_B T/u = 0.18$, where the pink cluster represents a closed shell connected through periodic-boundary-conditions, blue clusters are percolated partially grown shells, green clusters are partially grown shells which are not part of the percolated cluster, and white clusters are the disordered clusters, which are either freely diffusing or trapped inside the shell. (c) A percolated structure of partially grown shells is shown at $\phi = 0.08$ and $k_B T/u = 0.12$.

we observe disordered percolated clusters *P* (clusters which extend to the size of the simulation box⁴⁶), co-existing along with the comparatively smaller disordered clusters. Fig. 2(b) shows the snapshot of the system at $\phi = 0.4$ at $k_B T/u = 0.18$, where we observe a percolated network (blue spheres), along with closed structures (pink spheres), partially closed structures (green spheres) and small disordered clusters (grey spheres). For very low volume fraction $\phi = 0.08$ in *P*, we observe only the percolated network along with very few monomers in the system as shown in the snapshot of the system in Fig. 2(c).

In Fig. 3 we have shown $P(n_b)$, the probability distribution of n_b number of bonds of a subunit, as obtained from the different regions in the phase space. Fig. 3(a) is at $\phi = 0.4$ and $k_B T/u = 0.24$ where we observe only disordered clusters, the

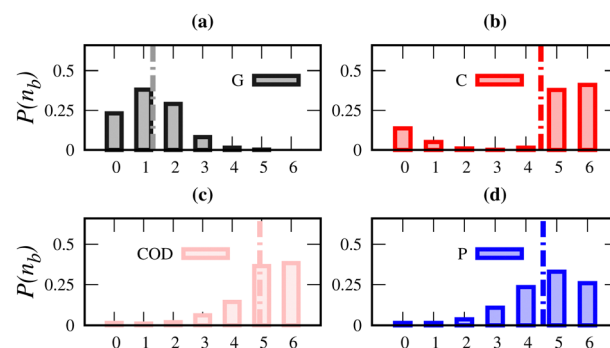


Fig. 3 Probability of the distribution of bonds of a subunit $P(n_b)$ and the dashed dotted line are the average bonded neighbours per particle $\langle n_b \rangle$ shown for the regions (a) G at $k_B T/u = 0.24$, $\phi = 0.4$ with $\langle n_b \rangle = 1.2$, (b) C at $k_B T/u = 0.16$, $\phi = 0.08$ with $\langle n_b \rangle = 4.7$, (c) COD at $k_B T/u = 0.14$, $\phi = 0.08$ with $\langle n_b \rangle = 4.8$, and (d) P at $k_B T/u = 0.12$, $\phi = 0.08$ with $\langle n_b \rangle = 4.7$.

majority of which are either monomer (0 bond), dimers (1 bond) or trimers (2 bonds) having the average number of bonds $\langle n_b \rangle = 1.2$ representing the G region. In the *C* region we observe that we have monomers and clusters having 5 and 6 bonds indicating the formation of complete closed structures, see Fig. 3(b). Once the nucleated shells are closed, they act as large gaseous particles, interacting only through the hardcore region, and coexist with smaller clusters. In Fig. 3(c), the monomers have been exhausted as the subunits are part of the clusters with each having 3 or more bonds. The higher nucleation rate leads to the growth of a large number of shells. Most of the shells remain partially closed as the number of subunits required to form a closed shell becomes greater than N . Similar behavior is observed experimentally for a system of virus capsids, where due to the high nucleation rates, the structure remains partially closed.³¹ On further reducing the temperature $k_B T/u = 0.08$ and $\phi = 0.08$, we observe percolated structures which will be a combination of partially closed structures connected to form system spanning clusters.

In Fig. 4, we have shown the structural properties calculated for the system corresponding to all the regions categorized in the T – ϕ plane of Fig. 2(a). The first peak of $G(r)$ in Fig. 4(a) is close to $r = d + \varepsilon = 1.25$, showing that the number of bonded neighbors is highest for the system in the COD and C regions,⁴⁷ followed by the P region. We can observe that for the C and COD regions the local ordering is almost the same as the closed shell structures are formed. For the P region, we observe that beyond $r/d > 3$ the system behaves liquid-like since the subunits are no longer showing long range order. The presence of cluster gas for the C and COD regions can be observed in the structure factor $S(q)$ shown in Fig. 4(b), where the presence of multiple closed as well as partially closed structures induces long range correlations in the system. For the P region, the $S(q)$ agrees with the C and COD region for $qd > 6$, while for smaller qd it behaves very similar to an irreversible DLCA percolated system.³⁶ In the case of the C and COD region, we can observe oscillations in $S(q)$ similar to the Fourier transform of a sphere of radius $R_s \sim 1.8$, which is the radius of the closed shell which is formed. For the G region as expected from the $S(q)$ calculation, we do not observe any long range order. To

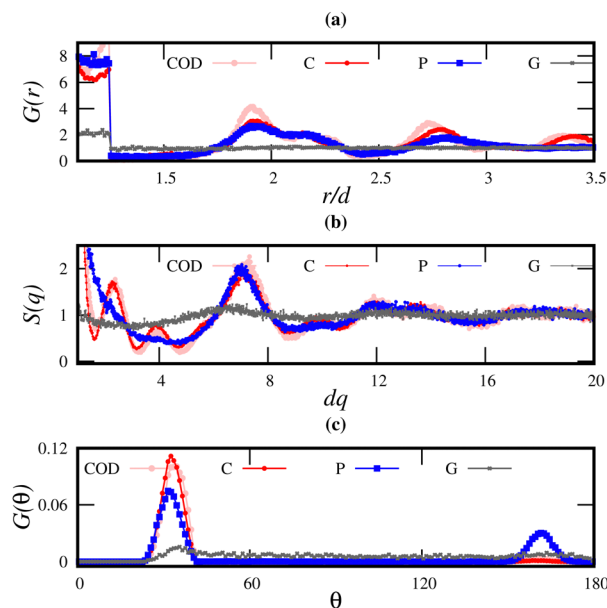


Fig. 4 (a) Radial distribution function $G(r)$ is shown for 4 regions identified in Fig. 2 where G at $k_B T/u = 0.24$, $\phi = 0.4$, C at $k_B T/u = 0.16$, $\phi = 0.08$, COD at $k_B T/u = 0.16$, $\phi = 0.28$, P at $(k_B T/u = 0.08, \phi = 0.12)$ for $\Omega^\circ = 74^\circ$, $\Delta\omega^\circ = 4.5$, $\varepsilon = 0.25$ and $p = 1.0$ (spherical hardcore). (b) The structure factor $S(q)$ is plotted as a function of qd , where q is the wave vector and (c) the angular distribution of bonded neighbors is shown corresponding to the above mentioned regions.

understand the orientation of the patch, which plays an important role in deciding the structure of the closed shell, we plotted the distribution of $G(\theta)$ (Fig. 4(c))¹⁸ where θ is the angle made by the patch vector of the subunit with respect to the bonded neighbor patch vector. In the C and COD region, we have all the patch vectors of the particles aligned in the same direction as we observe only one peak as expected for a closed structure. For the P region, we have peaks which agree with the C region and also a peak close to the $\theta = 180^\circ$. This indicates that particles are aligned in opposite orientations to each other thus making the percolated cluster disordered. For the G region, we observe the orientation as being uniform over almost all the θ values.

3.2 Kinetics of the shell growth

In order to study the shell growth, we have calculated the quantity $|r_{cm} - r_{cc}|$ as a function of time using the BCD simulation technique for an individual spherical shell in Fig. 5(a) and (b), having number of particles 166, $\varepsilon = 0.4$ and 167, $\varepsilon = 0.2$, respectively. Even though both the shells shown are formed for different ε , their $\Omega^\circ = 82^\circ$ and thus r_{cc}/b_1 of the close shell are the same, where b_1 is the average distance between the center of mass of bonded subunits. Here, we observe that $|r_{cm} - r_{cc}|$ goes down with increasing time because the cluster formed is closing in to form a spherical shell, and thereby it reaches a steady state value $< 10^{-3}$ at which point we consider that a closed shell is formed in the system. The reason for the fluctuation shown in Fig. 5(a) and (b) is due to bond rearrangements as well as the addition of new particles to the curved cluster. In Fig. 5(a) and (b) the different colors in the

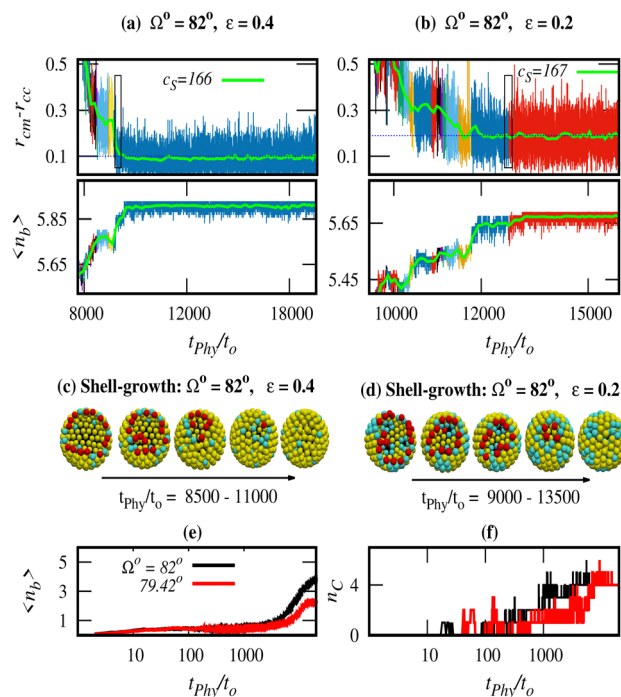


Fig. 5 (a) The growth kinetics of a single shell is studied by measuring the difference of the center of curvature and center of mass of a cluster as a function of time at $c_s = 166$, for $\Delta\omega^\circ = 4.5^\circ$, $\Omega^\circ = 82^\circ$, $\varepsilon = 0.4$ and $k_B T/u = 0.15$. The average $\langle |r_{cm} - r_{cc}| \rangle$ is shown as a solid line. The solid line reaches a steady state value corresponding to the closure of the spherical shell, as the radius of the center of mass and the center of curvature almost becomes the same. The fluctuation represented with different colors corresponds to adding subunits to the cluster through diffusion. Below, we show the corresponding change in the number of bond neighbors (n_b) per subunit for the cluster, which also reaches a steady state value when the shell closes. (b) Similar observation is shown for the cluster with number of subunits $c_s = 167$ obtained for the system with smaller b_1 having $\Delta\omega^\circ = 4.5^\circ$, $\Omega^\circ = 82^\circ$, $\varepsilon = 0.2$ and $k_B T/u = 0.13$ leading to the closing of the shell at higher $\langle |r_{cm} - r_{cc}| \rangle$. (c) A snapshot of shell growth is shown for $\Omega^\circ = 82^\circ$, $\varepsilon = 0.4$ with $c_s = 166$. (d) A snapshot of closed shell evolution of $\Omega^\circ = 82^\circ$, $\varepsilon = 0.4$ with $c_s = 167$. The red spheres are subunits with the number of bonded neighbors < 5 . The cyan and yellow spheres represent subunits with 5 and 6 bonded neighbors, respectively. (e) $\langle n_b \rangle$ the average number of bonded neighbors in the complete system is shown as a function of time t_{phys}/t_o at $\Delta\omega^\circ = 4.5^\circ$ and $\varepsilon = 0.2$ for different Ω° as indicated in the figure. The kinetics of aggregation show similarity to nucleation and growth-like phenomena. (f) The number of clusters having at least one subunit with 5 bonds n_C is shown with respect to time, which also grows along with $\langle n_b \rangle$.

fluctuation of $|r_{cm} - r_{cc}|$ indicate the addition of a new subunit through diffusion. We can also observe that without the addition of a new subunit, $\langle |r_{cm} - r_{cc}| \rangle$ (shown in the rectangular box) decreases, which is due to the rearrangement of the subunits by forming new bonds. The closure of a shell can happen either by the rearrangement of the bonds within the subunits or by the addition of new subunits through a diffusion process due to the finite width of the annular patches. The rearrangements of the bonds can be observed by an increasing n_b , which is the average number of bonded neighbors for a subunit. The subunit which is part of the new bond formation is shown as a red subunit (subunits with less than 5 neighbors)

in Fig. 5(c) and (d). For the same number of subunits, we can observe that the final structure has pentamers (cyan) distributed over the sphere with hexamers (yellow) close by while in Fig. 5(d) we observe pentamers forming subunits arranged together. When the spherical shell forms a closed structure, the fluctuation in $\langle |\mathbf{r}_{\text{cm}} - \mathbf{r}_{\text{cc}}| \rangle$ is only due to the diffusion of the subunits within the bonds. As soon as the average n_b reaches a steady state, $|\mathbf{r}_{\text{cm}} - \mathbf{r}_{\text{cc}}|$ also reaches a steady state as the spherical shell has closed. After the closed structure is formed, the subunits with 5 and 6 numbers of bonds continue to be transient, but the relative position of the subunit does not change or there is no structural rearrangement in the course of the simulation as shown in ESI,† I.

The average number of bonded neighbors n_b including all the clusters shows that for the time < 2000 the aggregation kinetics is the same for different Ω° , as shown in Fig. 5(e). For $\Omega^\circ = 82^\circ$ the number of subunits having 6 bonded neighbors increases faster than at $\Omega^\circ = 79^\circ$ as the volume over which the patchy subunits can form bonds also increases. Also, note that $\Omega^\circ = 82^\circ$ forms a bigger closed structure than 79° . This effect is also observed in Fig. 5(f) as a function of time, where we have plotted n_c , which is defined as the number of clusters with at least one subunit having 5 bonded neighbors. When the number of n_c is approximately 4, we observe a sudden proliferation in the number of clusters trying to form a closed structure, which is similar to nucleation and growth kind of phenomena. These phenomena can be observed in the ESI,† II.

3.3 Size, symmetry, and yield of the closed structures

The local structure over the surface of the shell was quantified using the radial distribution function $G(r)$. In Fig. 6(a), $G(r)$ is averaged over the center of mass of the subunits, which are only part of the shells and have the same number of c_s . Apart from the neighboring peak formed due to bonds formed with the neighbors, the surface of the shell is liquid-like or disordered. In Fig. 6(b), we have plotted the orientational correlation function $g(\theta)$,^{37,44} where θ is the angle between the unit vector associated with the patch of only the bonded neighbors. We observe that as the number of subunits increases, $\theta \rightarrow 0$ thus forming nearly parallel arrangement of the patch vectors. As the number of subunits associated with a shell increases with the same ε the diameter of the shell also increases. We also quantified the number of bonds associated with a subunit in 6(c) once the closed shell-like structure was formed. We observe that the majority of the subunits either have 5 (shown by cyan color in Fig. 1) or 6 (shown by yellow color in Fig. 1) bonded neighbors, which on average corresponds to pentagon and hexagon arrangements of the neighbors. The number of pentagons in a closed shell varies from 8–16 in the present study. These pentagons are the reason for closed shell formation in the system. As the number of hexagonal arrangements increases in a cluster, the diameter of the closed structure also increases. For smaller c_s the number of hexagons reduces and finally will have only pentagons (Fig. 6(b)). The 12 subunit system self assembles to form perfect icosahedral symmetry. We know that the structure formed with icosahedral symmetry

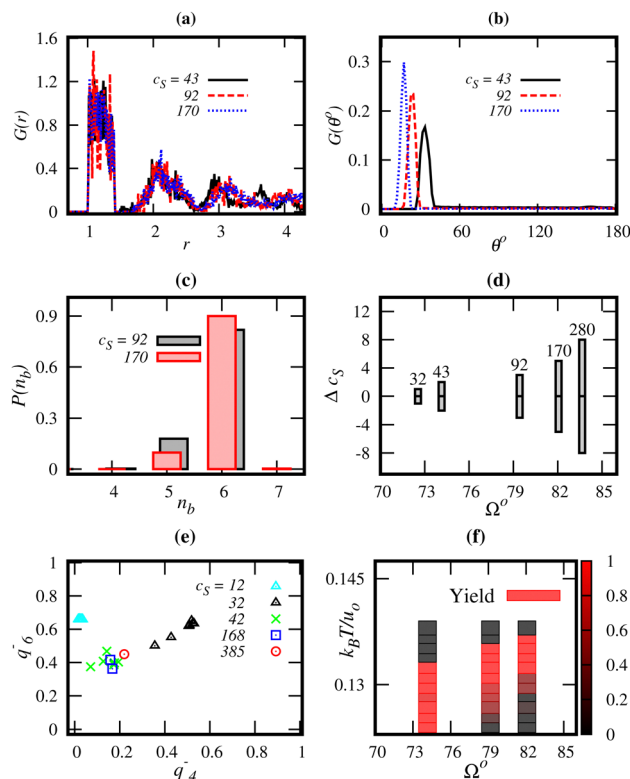


Fig. 6 (a) Radial distribution function $G(r)$ calculated over a closed shell, shown for $\Omega^\circ = 74.12^\circ$ (black), 79.6° (red), and 82° (blue) having the same $\Delta\omega^\circ = 3^\circ$ and $\varepsilon = 0.4$, corresponding to the different number of subunits for a closed shell as shown in the figure. (b) $G(\theta)$ the angular distribution of the bonded neighbors for a closed shell with different number of subunits as indicated. (c) Distribution of bonded neighbors $P(n_b)$ calculated over only the subunits which are part of the shell. (d) Subunit number variation in a cluster $\Delta c_s = |c_s - \bar{c}_s|$ for different Ω° values, where the average number of subunits in a cluster \bar{c}_s is shown in the figure. (e) Steinhardt order parameter is shown for the shell with a different number of subunits as indicated in the figure. (f) Variation in the yield (color coded) of perfectly closed shells, at different $k_B T/u$ for varying Ω° is shown at $\phi = 0.06$, $\varepsilon = 0.1$ and $\Delta\omega^\circ = 3^\circ$.

has a degenerate number of subunits, having exactly 12 pentagons if the structure is closed. In the present study, we calculated $\Delta c_s = c_s - \bar{c}_s$, where \bar{c}_s is the average number of subunits that is part of the closed structure, and we observe that the number of subunits in a closed structure does not follow icosahedral symmetry, as shown in Fig. 6(d). Thus, for $\bar{c}_s = 32$ we have $\Delta c_s = \pm 1$ and for $\bar{c}_s = 280$ we have $\Delta c_s = \pm 8$.

Although the $G(r)$ shows that the closed structure has a near liquid-like structure (see Fig. 6(a)), the bond order orientation parameter shows local order. We calculated the Steinhardt bond order orientation parameter \bar{q}_n as defined by Mosayebi *et al.*,⁹ which is given by

$$q_n = \left[\frac{4\pi}{2n+1} \sum_{m=-n}^n |\bar{q}_{nm}|^2 \sum_{m=-n}^n \right]^{\frac{1}{2}} \quad (4)$$

$$\bar{q}_{nm} = \langle Y_{1m}(\theta(\vec{r}), \phi(\vec{r})) \rangle \quad (5)$$

where $Y_{lm}(\theta, \phi)$ are spherical harmonics, and $\theta(\vec{r})$ and $\phi(\vec{r})$ are the polar and azimuthal angles respectively, with respect to the center of the cage.⁴⁸ When the maximum number of subunits being part of the closed shell was 12, we obtained the icosahedral symmetry as shown in Fig. 6(e) for spherical subunits, where we have shown q_6 as a function of q_4 for a closed shell containing a different number of subunits. For the simulation, we have observed that irrespective of the aspect ratio of the subunit, when the number of subunits is 12 we always obtained icosahedral symmetry. If the closed shell always shows icosahedral symmetry, then the closed shell can have only a degenerate number of subunits like 12, 32, 42, *etc.* Apart from this, the number of subunits having 5 neighbors (pentagon) in the system will be exactly 12 followed by all the other subunits having 6 neighbors (hexagon).

In the present study, we observe that the number of particles and the local symmetry of the system keep on changing, as shown in Fig. 6(e). Except for the number of subunits being 12, none of the closed shells show icosahedral symmetry. The number of pentagons (5 bonded neighbors) in all the closed structures that we obtained varies between 8 and 16 and it remains constant after the closed structure is formed. Also once the closed shell is formed we have observed transformation from 5 to 6 bonded neighbors and *vice versa* in the duration of our simulation. It has already been shown that when perturbations like flexibility of the bond are introduced to a perfect icosahedral symmetric closed structure, the symmetry is no longer required for the closed structure to be stable.⁹ This is very similar to the present system as the structure is formed from a random self-assembly process and the structure has flexible bonds as well depending on ε .

Yield is defined as the number of closed shells with respect to n_c . Thus, when there is only one spherical shell and the rest of the subunits are monomers, the yield will be unity. Fig. 6(f) shows the yield of the closed shell at different temperature, calculated at $\phi = 0.06$ for different values of Ω° . We observe that when the $\Omega^\circ = 74^\circ$, the yield is zero for $k_B T/u > 0.134$, because the clusters formed are smaller and the entropy contribution dominates, thereby not allowing closed shells. As we reduce $k_B T/u$, they do form many small closed structures. When we increase Ω° , the volume of the annular patch over which the subunit can form a bond increases and thus at higher $k_B T/u$ as well the system forms many closed structures with the same radius. On reducing $k_B T/u$ we observe that the enthalpic contribution dominates and many curved clusters are formed, which are not able to aggregate into a closed shell as expected. As we further increase Ω° , the region of high yield also reduces and also shifts towards higher $k_B T/u$. As $\Omega^\circ = 90^\circ$ we will never obtain a closed structure, as the patchy particles will prefer a flat surface instead of a curved surface.

The radius of the self assembled closed shell was quantified by calculating the radius from the center of mass and the center of curvature of the curved cluster. We will observe a distribution for the radius around a mean value, due to thermal fluctuation and finite width of the patch. Fig. 7(a) shows the distribution $P(r_s)$, which is the probability of occurrence of a spherical shell

with a particular radius r_s , having c_s subunits. The solid lines represent the radius distribution of the spherical shell as calculated from the center of mass calculation and the dotted line of the radius from the center of curvature calculation. As the number of subunits in the spherical shell increases, the radius of the shell also increases. When the angular width of the patch $\Delta\omega^\circ$ increases, the radius of the spherical shell decreases for the same temperature because the subunit can diffuse more freely within the bond, thus forming a compact structure, as shown in Fig. 7(b). The radius of the spherical shell increases with the decrease in the aspect ratio, as the excluded volume close to the annular patches increases when the aspect ratio decreases, such that an oblate spheroid will form a closed shell with larger radius.

Increasing the interaction range ε leads to a larger shell, as shown in Fig. 7(d). But it becomes more fluid-like, and larger pores can be observed between the subunits as they can diffuse within the bonds easily for higher ε . An interesting fact remains that the radius of the shell is independent of the volume fraction, as shown in Fig. 7(e). As we increase the volume fraction the number of shells formed increases while the radius remains constant, and also a few curved clusters will not be able to form closed structures, see Fig. 1(f). The same effect is also observed when we change temperature as well, see Fig. 7(f). By tuning Ω° we can control the radius of the shell to any desired radius. In Fig. 7(g) we have shown that irrespective of the aspect ratio of the particle the ratio r_{cc}/b_1 remains almost constant for the same $\Omega^\circ = 74^\circ$, where b_1 is the center of mass distance between the nearest subunit, deduced from the calculation of $G(r)$ of the closed structure irrespective of the aspect ratio of the subunit. The reason is that the radius of the shell is given by $\frac{r_{cc}}{b_1} \approx \frac{1}{2 \cos \Omega^\circ}$, as can be deduced from the inset of Fig. 7(h) where we have assumed that the subunits are connected together through the annular patches. The value of b_1 is obtained from the simulation, and it will always remain between $1 < b_1 < 1 + \varepsilon$. When we plot the radius of curvature of the cluster obtained from the simulation as a function of Ω° we observe that it follows the simple relation $1/2 \cos \Omega^\circ$ as shown by the solid line in Fig. 7(h). Only when $\Omega^\circ < 90^\circ$, the system will form closed structures.

The closed shells have been found to be monodisperse in terms of the radius. However, the annular patches used in the system have finite width $\Delta\omega$, which gives some degree of flexibility within the bond with directional constraints. In the *NVT* simulation, there is a finite possibility to be stuck in a metastable state. We have performed Gibbs Ensemble Monte Carlo simulation (GEMC) to verify that the system is in equilibrium and the structure formed agrees with the *NVT* simulations. To predict the possible radius of the equilibrium closed structures, we cannot use methods like variable shape simulation,^{49,50} as it requires translational degree of freedom for the subunits. The other way is to use the *NPT* ensemble on the surface of the sphere,⁵¹ but it requires prior knowledge of the exact number of particles required to close the shell. One other method can be a μPT ensemble performed over the

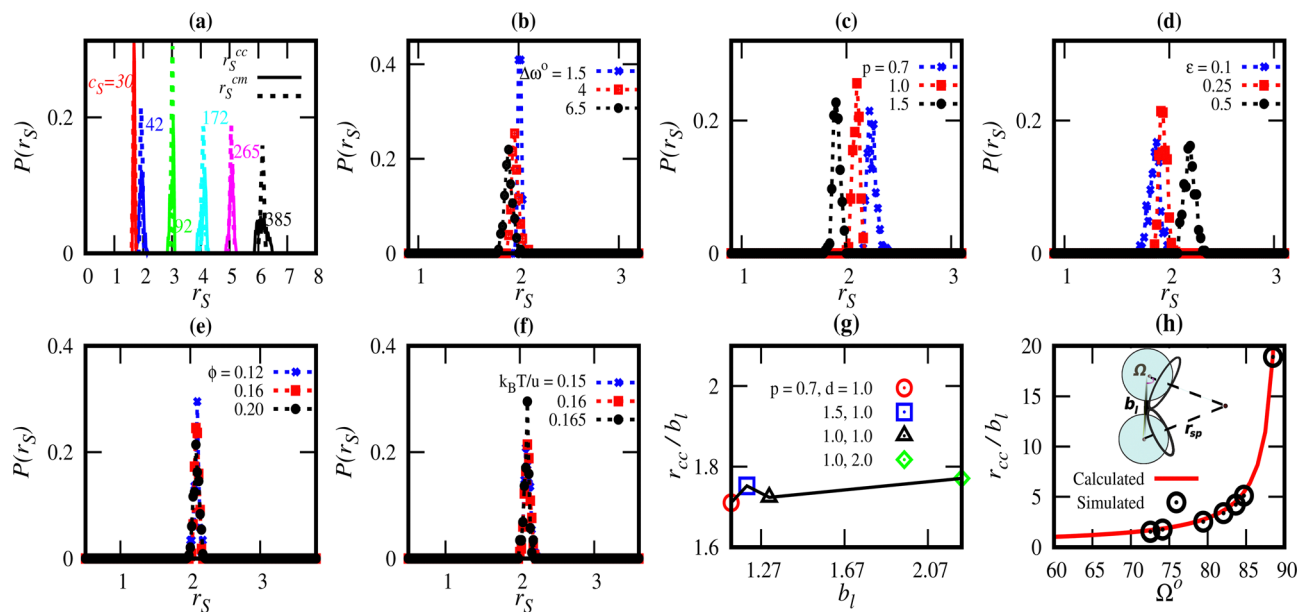


Fig. 7 (a) $P(r_s)$ is shown for different cluster sizes (obtained by different Ω° value, while keeping the rest of the potential parameters the same), measured from the center of mass (dotted line) and center of curvature of the shell (solid line). The position of the peak represents the radius of the shell, and the width shows the deviation from the spherical shape. (b) $P(r_s)$ is shown for different $\Delta\omega^\circ$ (calculated at $\Omega^\circ = 74^\circ$ and $\varepsilon = 0.25$) values, showing the effect of patch width over the size and shape of the shell. (c) $P(r_s)$ is shown for different hard-core shapes as indicated in the figure, calculated for $\Omega^\circ = 74^\circ$, $\varepsilon = 0.25$ and $\Delta\omega^\circ = 3^\circ$. (d) The effect of the patch range is shown for different ε as shown in the figure at $\Omega^\circ = 74^\circ$ and $\Delta\omega^\circ = 4.5^\circ$. (e) $P(r_s)$ is shown for the system at different ϕ (as indicated in the figure) while keeping all the other parameters the same. (f) The effect of temperature over $P(r_s)$ is shown for the shells obtained by using the same parameters. (g) The ratio r_{cc}/b_l where b_l is the distance of the center of mass of a neighboring subunit for different aspect ratios and diameters of the subunit as indicated in the figure for $\Omega^\circ = 74^\circ$. The solid line is a guide to the eye. (h) Effect of Ω° over r_{cc}/b_l , showing the latter dominantly controlled by Ω° . The solid line is given by $\frac{1}{2 \cos \Omega^\circ}$.

surface of the sphere, where confinement and a fixed number of particles can ensure the convergence of the system. In this method, there is a finite probability that before reaching the minimum energy configuration, the size of the system in the fluid phase would start diverging to maintain constant μ and P , thus making the μPT ensemble not a good method⁵² for the present work.

Gibbs ensemble Monte Carlo (GEMC)⁵³ is implemented on the surface of the sphere. This method does not account for the fluctuations or deviation in shape, away from the sphere. In this method, we take two spheres of same radius and randomly distribute the subunit over the surface of the sphere, which are randomly moved and rotated on the surface of the sphere. This is followed by an attempt to change the surface area of the sphere, such that the total surface area of both spheres together remains constant. Each of these steps are accepted by a probability as given in Appendix I. When an equilibrium is reached, one sphere will give us the radius as well as the number of subunits of the closed shell at a particular temperature. While the one in the other sphere will contain disordered clusters on the surface, see Appendix I. We performed Gibbs ensemble simulation over the surface of a sphere for a number of configurations by changing the temperature. We found that the method predicts the r_{cc}/b_l vs. Ω° relation as the same (shown as blue triangular points in Fig. 8) as it has been obtained in the NVT simulation (shown as a blue triangular

point in Fig. 8). Here we observe that even in the GEMC simulation, the size of the cluster is favored, which corresponds to the relation $r_{cc}/b_l = \frac{1}{2 \cos \Omega^\circ}$. Although going for the higher value of Ω° , we observe deviation from the red line (Fig. 8). It happens due to the finite width of the annular patch ($\Delta\omega = 4.5^\circ$). As we increase Ω° , the size of the shell becomes very sensitive with Ω° and diverges close to $\Omega^\circ = 90^\circ$.

4 Discussion and conclusion

Making annular patches is possible through experiments, as patchy interactions have been created by grafting polymers onto complicated asymmetric building blocks at desired locations.⁵⁴ Most of the closed structures generated experimentally have been created by tweaking the interaction between protein molecules⁵⁵ or virus subunits,⁵⁶ which restricts the radius of the cages formed. One of the challenges that need to be addressed is the maximum size over which these structures can be formed. In the present model of annular patches, the size constraint challenge is addressed. In addition, the model also creates monodisperse closed shells in terms of the radius for low concentration. For intermediate concentrations, nanocontainer-like structures emerge. These structures will find applications in vaccine production, acting as nanoreactors, drug delivery systems, etc. By restricting the number of bonds

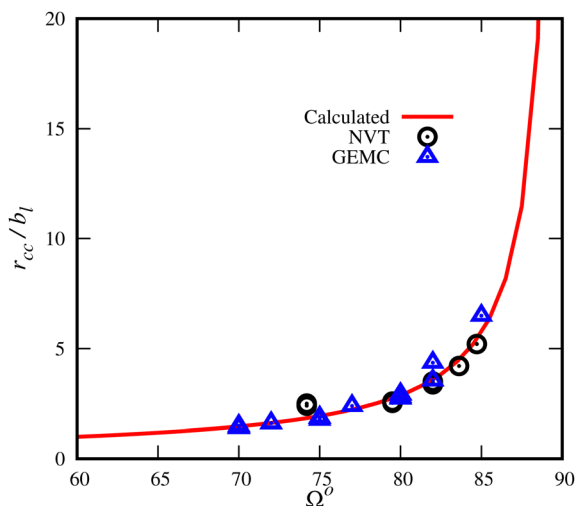


Fig. 8 The size of the shells predicted by GEMC (blue triangles) and compared with the same obtained by using NVT (black circles). The solid line shows the simple relation $1/2 \cos \Omega^\circ$ between the patch angle of ω and the size of the shell.

formed per patch it is possible to engineer different morphologies for the clusters formed, including the closed structures of different geometry through the self-assembly route. This simple potential proposed in the present work may also provide insight into understanding more complex structures like the virus.

Conflicts of interest

There are no conflicts to declare.

Appendix

To perform the GEMC simulation on the surface of the sphere, we took two spheres of surface area A_1 and A_2 . Then the N number subunits are randomly distributed on the surface of the spheres with area fraction defined by $\phi_A = 4\pi R_s^2$, where R_s is the radius of the spheres. $2N$ particles are randomly chosen such that each particle will undergo one translational movement and one rotation in each simulation step. The subunit moves on the surface of the sphere in the translational step. While in the rotational step the patch vector of the subunit undergoes a rotation in a random direction. Following the subunits movement, the surface areas of the spheres are changed randomly in small steps, such that the total area of the two spheres $A_t = A_1 + A_2$ remains constant throughout the simulation. After changing the area, the position of the particles is re-scaled with the factor R'_s/R_s , where R'_s is the radius of the sphere after the change in the area. The change in radius is accepted according to the Gibbs ensemble criteria,⁵⁷ given as,

$$\text{acceptance}(A_1 + A_2 \rightarrow A'_1 + A'_2) = \min[\exp[-\beta(\Delta E)], 1] \quad (6)$$

Such that,

$$\Delta E = \Delta U_1 + \Delta U_2 - N_1 \ln \frac{A'_1}{A_1} - N_2 \ln \frac{A'_2}{A_2} \quad (7)$$

where ΔU_1 and ΔU_2 are the change in energy of the first and second sphere. Following the volume change movement, we also swap subunits from one spherical surface to the other, such that the total number of the subunit on both the spheres together remains a constant and equal to N . A subunit is randomly chosen and deleted from one sphere and inserted into another one by assigning a random orientation of the patch vector and at a position randomly chosen over the surface of the sphere on which the subunit is being placed. The change in energy in both the spheres is calculated ($\Delta U_3 + \Delta U_4$) where the criteria for the acceptance of swapping the particle⁵⁷ is given as,

$$\text{acceptance}(1 \rightarrow 2) = \min[\exp[-\beta(\Delta E)], 1] \quad (8)$$

Such that,

$$\Delta E = \Delta U_3 + \Delta U_4 + \ln \frac{A_1 \cdot N_2 + 1}{A_2 \cdot N_1} \quad (9)$$

Note that it is better to start with a number of subunits of about 5 times the number obtained from the NVT ensemble for a closed shell at the right temperature for faster convergence. To show the convergence, we start the system with $N_1 + N_2 = 200$, at $\phi_A = 0.1$. The system with sphere size close to the final configuration ($N_1 + N_2 = 200$) converges to $N_s \sim 48$ (see Fig. 9(a)) and $R_s \sim 1.8$ (see Fig. 9(b)) as obtained from the NVT simulation. The second spheres have a higher R_s and N_s , which represents fluid-like behavior with sparsely distributed clusters on the sphere.

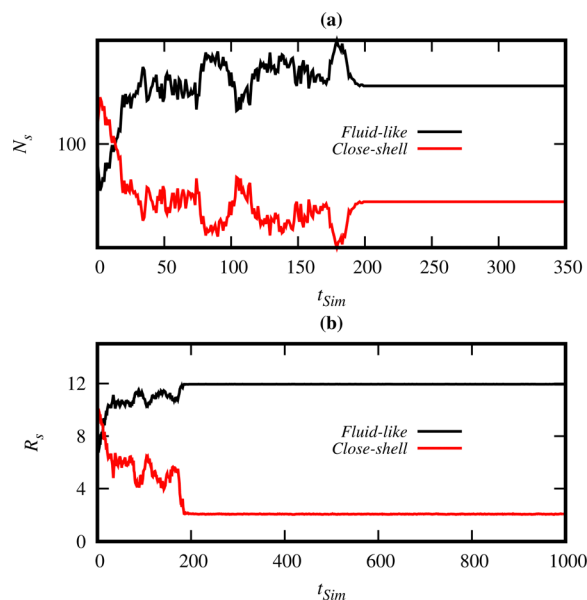


Fig. 9 (a) Variation in N_s and (b) variation in R_s is shown, where the red line represents Sphere 1 and the black line represents Sphere 2 of a particular ensemble. The system is kept at $\phi_A = 0.1$, $k_B T/u = 0.14$ having patch properties $\Omega^\circ = 74^\circ$, $\Delta\omega^\circ = 4.5$, $\varepsilon = 0.25$ and $p = 1.0$.

Acknowledgements

We would like to acknowledge the UGC-CSIR funding agency for the fellowship. SBB acknowledges the partial support from DST-SERB India (project no. CRG/2019/000580).

Notes and references

- 1 Y. Hsia, J. B. Bale, S. Gonen, D. Shi, W. Sheffler, K. K. Fong, U. Nattermann, C. Xu, P.-S. Huang, R. Ravichandran, S. Yi, T. N. Davis, T. Gonen, N. P. King and D. Baker, *Nature*, 2016, **535**, 136–139.
- 2 D. N. Shurpik, L. I. Makhmutova, K. S. Usachev, D. R. Islamov, O. A. Mostovaya, A. A. Nazarova, V. N. Kizhnyayev and I. I. Stoikov, *Nanomaterials*, 2021, **11**, 947.
- 3 J. H. Swisher, L. Jibril, S. H. Petrosko and C. A. Mirkin, *Nat. Rev. Mater.*, 2022, **7**, 428–448.
- 4 E. Shchukina and D. G. Shchukin, *Langmuir*, 2019, **35**, 8603–8611.
- 5 C. Sigl, E. M. Willner, W. Engelen, J. A. Kretzmann, K. Sachenbacher, A. Liedl, F. Kolbe, F. Wilsch, S. A. Aghvami, U. Protzer, M. F. Hagan, S. Fraden and H. Dietz, *Nat. Mater.*, 2021, **20**, 1281–1289.
- 6 R. Gao, H. Tan, S. Li, S. Ma, Y. Tang, K. Zhang, Z. Zhang, Q. Fan, J. Yang, X.-E. Zhang and F. Li, *Proc. Natl. Acad. Sci. U. S. A.*, 2022, **119**, e2104964119.
- 7 K. Kamata, Y. Lu and Y. Xia, *J. Am. Chem. Soc.*, 2003, **125**, 2384–2385.
- 8 A. S. Sussha, F. Caruso, A. L. Rogach, G. B. Sukhorukov, A. Kornowski, H. Möhwald, M. Giersig, A. Eychmüller and H. Weller, *Colloids Surf., A*, 2000, **163**, 39–44.
- 9 M. Mosayebi, D. K. Shoemark, J. M. Fletcher, R. B. Sessions, N. Linden, D. N. Woolfson and T. B. Liverpool, *Proc. Natl. Acad. Sci. U. S. A.*, 2017, **114**, 9014–9019.
- 10 D. C. Rapaport, *Phys. Rev. E: Stat., Nonlinear, Soft Matter Phys.*, 2004, **70**, 051905.
- 11 R. Zandi, D. Reguera, R. F. Bruinsma, W. M. Gelbart and J. Rudnick, *Proc. Natl. Acad. Sci. U. S. A.*, 2004, **101**, 15556–15560.
- 12 S. Schyck, J.-M. Meijer, L. Baldauf, P. Schall, A. V. Petukhov and L. Rossi, *JCIS Open*, 2022, **5**, 100037.
- 13 A. Gangrade, N. Stephanopoulos and D. Bhatia, *Nanoscale*, 2021, **13**, 16834–16846.
- 14 S. Dey, C. Fan, K. V. Gothelf, J. Li, C. Lin, L. Liu, N. Liu, M. A. D. Nijenhuis, B. Saccà, F. C. Simmel, H. Yan and P. Zhan, *Nat. Rev. Methods Primers*, 2021, **1**, 13.
- 15 H. Wang, L.-P. Zhou, Y. Zheng, K. Wang, B. Song, X. Yan, L. Wojtas, X.-Q. Wang, X. Jiang, M. Wang, Q.-F. Sun, B. Xu, H.-B. Yang, A. C.-H. Sue, Y.-T. Chan, J. L. Sessler, Y. Jiao, P. J. Stang and X. Li, *Angew. Chem., Int. Ed.*, 2021, **60**, 1298–1305.
- 16 A. Michelson, B. Minevich, H. Emamy, X. Huang, Y. S. Chu, H. Yan and O. Gang, *Science*, 2022, **376**, 203–207.
- 17 E. Golub, R. H. Subramanian, J. Esselborn, R. G. Alberstein, J. B. Bailey, J. A. Chiong, X. Yan, T. Booth, T. S. Baker and F. A. Tezcan, *Nature*, 2020, **578**, 172–176.
- 18 I. Malhotra and S. B. Babu, *J. Chem. Phys.*, 2019, **151**, 084901.
- 19 I. Malhotra and S. B. Babu, *J. Phys.: Condens. Matter*, 2020, **32**, 355101.
- 20 A. Neophytou, D. Chakrabarti and F. Sciortino, *Nat. Phys.*, 2022, **18**, 1248–1253.
- 21 Z. Zhang and S. C. Glotzer, *Nano Lett.*, 2004, **4**, 1407–1413.
- 22 M. Liu, X. Zheng, V. Grebe, D. J. Pine and M. Weck, *Nat. Mater.*, 2020, **19**, 1354–1361.
- 23 S. Lee, T. Vo and S. C. Glotzer, *Nat. Chem.*, 2023, **15**, 905–912.
- 24 D. E. P. Pinto, P. Šulc, F. Sciortino and J. Russo, *Proc. Natl. Acad. Sci. U. S. A.*, 2023, **120**, e2219458120.
- 25 E. Bianchi, P. D. J. van Oostrum, C. N. Likos and G. Kahl, *Curr. Opin. Colloid Interface Sci.*, 2017, **30**, 8–15.
- 26 P. Buzón, S. Maity, P. Christodoulis, M. J. Wiertsema, S. Dunkelbarger, C. Kim, G. J. Wuite, A. Zlotnick and W. H. Roos, *Sci. Adv.*, 2021, **7**, eabg0811.
- 27 J. Rong, Z. Niu, L. A. Lee and Q. Wang, *Curr. Opin. Colloid Interface Sci.*, 2011, **16**, 441–450.
- 28 P. Buzón, S. Maity and W. H. Roos, *Wiley Interdiscip. Rev.: Nanomed. Nanobiotechnol.*, 2020, **12**, e1613.
- 29 K. Wu, T. K. Ronson, P. Su, Z. Chen, L. Goh, A. W. Heard, X. Li, F. Klautzsch, C. A. Schalley and M. Vinković, *et al.*, *Nat., Synth.*, 2023, 1–9.
- 30 W. Li, Y. Liu, G. Brett and J. D. Gunton, *Soft Matter*, 2012, **8**, 6027–6032.
- 31 R. F. Garmann, A. M. Goldfain and V. N. Manoharan, *Proc. Natl. Acad. Sci. U. S. A.*, 2019, **116**, 22485–22490.
- 32 R. Zandi, D. Reguera, R. F. Bruinsma, W. M. Gelbart and J. Rudnick, *Proc. Natl. Acad. Sci. U. S. A.*, 2004, **101**, 15556–15560.
- 33 S. Babu, J.-C. Gimel, T. Nicolai and C. De Michele, *J. Chem. Phys.*, 2008, **128**, 204504.
- 34 A. Prabhu, S. B. Babu, J. S. Dolado and J.-C. Gimel, *J. Chem. Phys.*, 2014, **141**, 024904.
- 35 V. A. Varma, I. Malhotra and S. B. Babu, *PRE*, 2022, **106**, 014602.
- 36 S. Babu, J. C. Gimel and T. Nicolai, *Eur. Phys. J. E: Soft Matter Biol. Phys.*, 2008, **27**, 297–308.
- 37 I. Malhotra and S. B. Babu, *Pure Appl. Chem.*, 2018, **90**, 1085–1098.
- 38 Z. Shireen and S. B. Babu, *J. Chem. Phys.*, 2017, **147**, 054904.
- 39 Z. Shireen and S. B. Babu, *Soft Matter*, 2018, **14**, 9271–9281.
- 40 Z. Shireen, T. Curk, C. Brandl and S. B. Babu, *ACS Omega*, 2023, **8**, 37225–37232.
- 41 S. Babu, J. C. Gimel and T. Nicolai, *J. Chem. Phys.*, 2006, **125**, 184512.
- 42 S. Babu, J. C. Gimel and T. Nicolai, *J. Chem. Phys.*, 2007, **127**, 054503.
- 43 S. Babu, J.-C. Gimel and T. Nicolai, *J. Chem. Phys.*, 2009, **130**, 064504.
- 44 V. A. Varma, Kritika, J. Singh and S. B. Babu, *Adv. Theory Simul.*, 2023, 2200666.
- 45 D. Richard, C. P. Royall and T. Speck, *J. Chem. Phys.*, 2018, **148**, 241101.
- 46 H. He and M. F. Thorpe, *Phys. Rev. Lett.*, 1985, **54**, 2107.

- 47 W. Kranendonk and D. Frenkel, *Mol. Phys.*, 1988, **64**, 403–424.
- 48 P. J. Steinhardt, D. R. Nelson and M. Ronchetti, *Phys. Rev. B: Condens. Matter Mater. Phys.*, 1983, **28**, 784.
- 49 L. Fillion, M. Marechal, B. van Oorschot, D. Pelt, F. Smallenburg and M. Dijkstra, *Phys. Rev. Lett.*, 2009, **103**, 188302.
- 50 T. Vissers, Z. Preisler, F. Smallenburg, M. Dijkstra and F. Sciortino, *J. Chem. Phys.*, 2013, **138**, 164505.
- 51 Y. Li, H. Miao, H. Ma and J. Z. Chen, *Soft Matter*, 2013, **9**, 11461–11466.
- 52 D. Frenkel and B. Smit, *Understanding molecular simulation*, Elsevier, 2001, vol. 1.
- 53 A. Z. Panagiotopoulos, N. Quirke, M. Stapleton and D. Tildesley, *Mol. Phys.*, 1988, **63**, 527–545.
- 54 A. Kim, T. Vo, H. An, P. Banerjee, L. Yao, S. Zhou, C. Kim, D. J. Milliron, S. C. Glotzer and Q. Chen, *Nat. Commun.*, 2022, **13**, 6774.
- 55 N. P. King, J. B. Bale, W. Sheffler, D. E. McNamara, S. Gonen, T. Gonen, T. O. Yeates and D. Baker, *Nature*, 2014, **510**, 103–108.
- 56 G. Indelicato, P. Cermelli and R. Twarock, *Phys. Rev. E*, 2022, **105**, 064403.
- 57 A. Z. Panagiotopoulos, N. Quirke, M. Stapleton and D. J. Tildesley, *Mol. Phys.*, 1988, **63**, 527–545.